Electric Field Control of the Skyrmion Hall Effect in Piezoelectric-Magnetic Devices

Mouad Fattouhi,* Felipe García-Sánchez, Rocío Yanes, Víctor Raposo, Eduardo Martínez, and Luis Lopez-Diaz†

Department of Applied Physics, University of Salamanca, Plaza de la Merced, 37008 Salamanca, Spain

(Received 16 July 2021; accepted 24 September 2021; published 20 October 2021)

Relying on both electromechanical and micromagnetic simulations, we propose a method to control the trajectory of current-driven skyrmions using an electric field in hybrid piezoelectric-magnetic systems. By applying a voltage between two lateral electrodes, a transverse strain gradient is created, as a result of the nonuniform electric field profile in the piezoelectric material. Due to magnetoelastic coupling, this transverse gradient leads to a lateral force on the skyrmions that can be used to suppress the skyrmion Hall angle for any given current density, if a proper voltage is applied. We show that this method works under realistic conditions, such as the presence of disorder in the ferromagnet, and that skyrmion trajectories can be controlled with moderate voltages. Moreover, our method allows the maximum current density that can be injected before the skyrmion is annihilated at the nanostrip edge to be increased, which leads to an increase in the maximum achievable velocities.

DOI: 10.1103/PhysRevApplied.16.044035

I. INTRODUCTION

Since their observation in 2009 [1], magnetic skyrmions have attracted a lot of attention, not only from the point of view of fundamental research, but also because they present some features, such as small size, topological protection, or being sensitive to moderate current densities, that make them attractive for the development of the next generation of spintronic devices. In this sense, different skyrmion-based devices have been proposed, such as logic gates [2–5], magnetic memories [6,7], artificial neuron spikes [8,9], or microwave detectors [10]. The potential success of these devices relies on our capacity for nucleating, stabilizing, and controlling the motion of skyrmions in an energy-efficient way.

Magnetic skyrmions can be moved using spin-polarized electrical currents [11], anisotropy gradients [12], strain gradients [13], surface acoustic waves [14], magnetic field gradients [15], spin waves [16], temperature gradients [17], etc. Regardless of the nature of the driving force, the skyrmion trajectory is not parallel to the direction of this force, but it deviates a certain angle from it [18], a phenomenon usually referred to as the skyrmion Hall effect (SKHE) [19–22]. This universal phenomenon is due to the gyrotropic nature of magnetization dynamics, which leads to the appearance of a force on the skyrmion perpendicular to the driving one, the so-called Magnus force [23]. This force is detrimental for the design of skyrmion-based devices, such as racetrack memories, where skyrmions are intended to follow a straight path along the nanostrip. Consequently, different approaches are proposed to avoid it. For example, the SKHE should not be present in antiferromagnets [24,25] because the skyrmion's gyrovector is cancelled out, but the nucleation of isolated skyrmions in antiferromagnets has not been reported so far. The SKHE is also absent in synthetic antiferromagnets (SAFs) [26] because the two interlayer-coupled skyrmions exhibit antiparallel Magnus forces that cancel each other out, but, although isolated skyrmions are stabilized in SAFs [27], their controlled motion by an electrical current or by any other means is still in a premature state [28]. Other more exotic textures, like magnetic skyrmioniums, should also move without the SKHE, since their topological charge is roughly zero [29,30].

Tuning the skyrmion intrinsic properties is not the only way to suppress the SKHE. An alternative approach is based on inducing an external force to compensate for the Magnus force. Different methods are proposed along this line. In fact, in narrow strips, the skyrmion is repelled by the edges, and this repulsive transverse force is useful for maintaining skyrmion movement straight along the track [31]. On the other hand, it is shown that, by engineering Rashba and Dresselhaus spin-orbit couplings, it is possible to suppress the skyrmion Hall angle for both Néel skyrmions and Bloch antiskyrmions [32]. Heavy-metal layers with reduced symmetry in chiral multilayers are also a route to minimize the skyrmion Hall angle and to

*mfa@usal.es
†lld@usal.es

maximize its speed via partial current polarization in such systems [33]. In any case, other methods, providing more freedom and versatility to manipulate skyrmion motion, are desirable to develop alternative technologies. In the present work, we propose an approach for this purpose. It is based on a transverse-voltage-induced mechanical excitation of a piezoelectric layer attached to the ferromagnetic nanostrip, which, due to magnetoelastic(ME) coupling, creates a transverse force on the skyrmion that can be used to totally suppress the skyrmion Hall angle and to increase its velocity.

In the next section, we present and discuss the results on which our proposal is based. We will first study the electromechanical response of our system and characterize, both qualitatively and quantitatively, the strain profile transferred to the ferromagnetic nanostrip along which the skyrmions move. Second, we use both micromagnetic simulations and Thiele's model [34] to show that this strain profile creates a transverse force on the skyrmion that can be used to correct its trajectory when driven by a current flowing parallel to the nanostrip. Moreover, we derive the conditions to suppress the skyrmion Hall angle for any given value of current density. In the last part, we show that our approach works under realistic conditions, such as the presence of disorder in the sample, and that it can be used to increase the maximum achievable skyrmion velocities.

II. RESULTS AND DISCUSSION

A sketch of the device proposed is presented in Fig. 1(a), where skyrmions move along a perpendicularly magnetized ferromagnetic (FM) racetrack driven by a current passing through an adjacent heavy metal (HM). The HM/FM/oxide trilayer is grown on top of a thick piezoelectric (PZ) film with two extended lateral electrodes on top of it, as shown in the figure. The basic idea of our proposal is that, due to magnetoelastic coupling, the strain created in the system when a voltage is applied between these two electrodes leads to a force on the skyrmions that can be used to control their lateral motion.

Electromechanical simulations are performed using COMSOL Multiphysics [35]. As a piezoelectric material, we use PZT-4 (lead zirconate titanate) of dimensions $\ell_{PZ} = 1200$ nm , $w_{PZ} = 1000$ nm, and $t_{PZ} = 100$ nm [see Fig. 1(a)], whereas for the HM/FM/oxide we consider Pt(2 nm)/$Co_{20}Fe_{60}B_{20}$(1 nm)/MgO(1 nm) with lateral dimensions of $\ell_{FM} = 1024$ nm, $w_{FM} = 500$ nm, and the following values for the Young's modulus and Poisson ratio: $Y_{Pt} = 154$ GPa, $\nu_{Pt} = 0.385$ [36], $Y_{Co\text{-}Fe\text{-}B} = 162$ GPa, $\nu_{Co\text{-}Fe\text{-}B} = 0.3$ [37], $Y_{MgO} = 270$ GPa, and $\nu_{MgO} = 0.35$ [38]. When calculating the electromechanical response, we assume that the PZ bottom surface is clamped to the substrate, and we consider the conductive nature of both FM and HM layers.

Figure 1(b) shows the electric field lines in the PZ material in the device cross section. As can be observed, the field lines leak into the HM layer due to its conductive nature, yielding a highly nonuniform field pattern. In particular, we note the profile of the out-of-plane component, E_z, along the PZ/HM interface in the transversal direction, which is plotted in Fig. 1(c) for an applied voltage of 10 V between the electrodes. As can be observed, the field strength is maximum at the edges, but it points in opposite directions, and a gradual nonlinear transition between these two extreme values is obtained, as we move from one edge to the other. The profile along the central region,

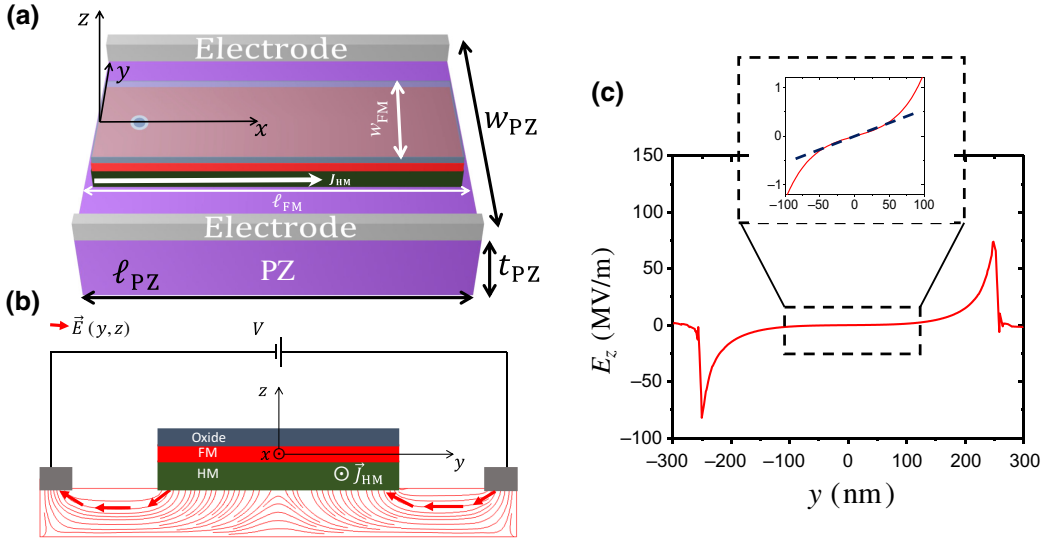

FIG. 1. (a) Schematic representation of the simulated device. (b) Device cross section showing the electric field lines in the PZ substrate. (c) Profile of the vertical component, E_z, along the PZ/HM interface. Inset is a magnification of the profile in the central region of the nanostrip.

shown in the inset of Fig. 1(c), is approximately linear with a slope of $(dE_z/dy) \sim 10$ V/μm^2.

The strain distribution in the device, as the response of the PZ substrate to the electric field, is also calculated with COMSOL Multiphysics [35]. In particular, Fig. 2(a) shows the profile of the strain component, ε_{yy}, transferred from the PZ layer to the FM for different widths of the PZ substrate. As can be observed, a smooth quasi-linear profile changing sign across the central point of the FM is obtained in all cases. This strain profile can be understood by looking at the electric field in Fig. 1(c) and considering that, in the absence of external stress, we have $\varepsilon_{yy} = d_{13}E_z$, where $d_{13} = -1.23 \times 10^{-10}$ C N^{-1} in our case [35]. Other factors, such as residual stresses due to substrate clamping [39], also affect the strain, but their contribution is small. In Fig. 2(b), the strain gradient at the center ($y = 0$) as a function of w_{PZ} is plotted. The gradual decrease is a consequence of the electric field scaling with the inverse of the distance between electrodes (w_{PZ}^{-1}).

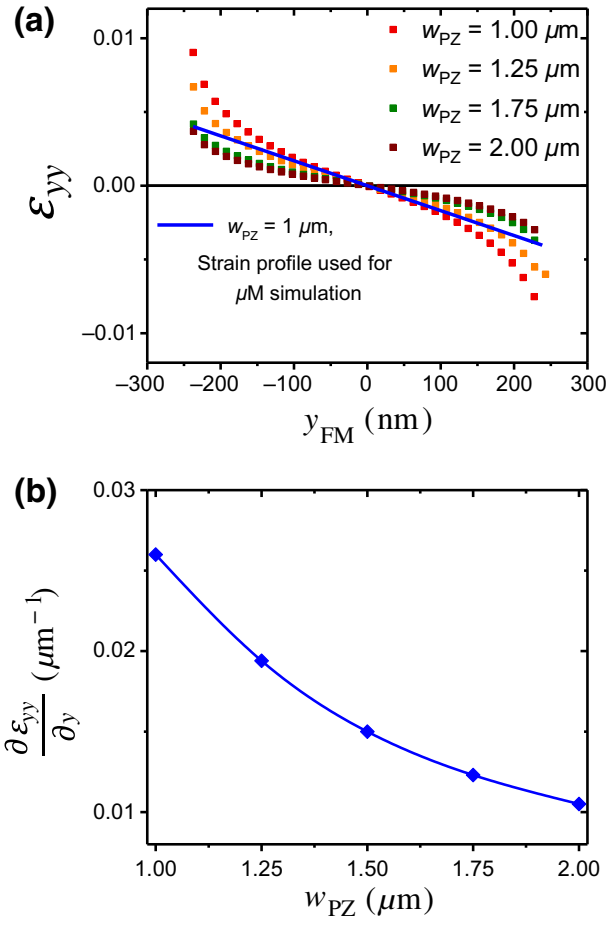

FIG. 2. (a) Elastic strain (ε_{yy}) profile transferred to the FM layer across the central region for different PZ layer widths. Blue line represents a linear profile obtained by extrapolating the slope at the origin ($y = 0$) for $w_{PZ} = 1$ μm. (b) Strain gradient in the center of the FM ($y = 0$) for different PZ-layer widths, w_{PZ}. Voltage, $V = 10$ V, between the electrodes is applied in all cases.

To sum up, our electromechanical simulations show that, by applying moderate voltages between the electrodes, it is possible to create strain gradients in the central region of the FM racetrack in the order of 10^{-2} μm^{-1}. Moreover, the magnitude of the gradient can be controlled with the applied voltage and the distance between the electrodes.

Once we characterize the mechanical response of the device, in what follows, we will investigate how this can be used to control the lateral motion of skyrmions in our system. To do that, we perform micromagnetic simulations of a skyrmion driven by a current flowing through the HM layer [Fig. 1(a)] and in the presence of a transverse strain gradient, $d\varepsilon_{yy}/dy$. Simulations are carried out using a graphical processing unit (GPU)-based in-home-modified version of Mumax3 that includes a magnetoelastic contribution to the effective field [13,40] given by

$$\vec{H}_{ME} = \frac{1}{\mu_0 M_s}\sigma_{ij}\frac{\delta \varepsilon_{ij}^m}{\delta \vec{m}}, \tag{1}$$

where σ_{ij} and ε_{ij}^m are the stress and magnetic strain tensors, respectively; M_s is the saturation magnetization; μ_0 is the vacuum permeability; and $\vec{m}(r,t) = \vec{M}(r,t)/M_s$ is the reduced magnetization. The Landau-Lifshitz-Gilbert dynamic equation is augmented with Slonczewski-like spin-orbit torque that takes into account the contribution of the current flowing through the HM [41,42]. The following material parameter values, typical of oxide/Co-Fe-B/HM multilayers [43–47], are used in the micromagnetic simulations: $A_{ex} = 20$ pJ/m (exchange stiffness), $M_s = 1$ MA/m (saturation magnetization), $K_u = 0.8$ MJ/m^3 (uniaxial anisotropy), $D_{int} = 1.8$ mJ/m^2 (interfacial Dzyaloshinskii-Moriya), $\lambda_s = 3.7 \times 10^{-5}$ (magnetostriction), $\alpha = 0.3$ (damping constant), and $\theta_{SH} = -0.33$ (spin Hall angle).

Figure 3 shows the effect of the transversal strain gradient on skyrmion dynamics. In Fig. 3(b), we plot the skyrmion trajectory for an applied current density of 10 GA/m^2 and different values of the strain gradient, $d\varepsilon_{yy}/dy$. As can be observed, the skyrmion Hall angle decreases as the strain gradient is increased. This trend is confirmed in Fig. 3(c), where the skyrmion Hall angle is plotted as a function of the strain gradient for three different applied current densities, showing a monotonous decrease in all cases. The strain gradient, therefore, creates a force that pushes the skyrmion towards regions of higher strain. The origin of this force, which was analyzed in Ref. [13], lies in the fact that the skyrmion energy is reduced as the strain increases. This force, $\vec{F}_{el}$, is schematically represented in Fig. 3(a) (green) together with the driving force exerted by the current $\vec{F}_{SHE}$ (yellow). Their associated skyrmion Magnus forces, $\vec{F}_{Magnus}$ and $\vec{F}'_{Magnus}$,

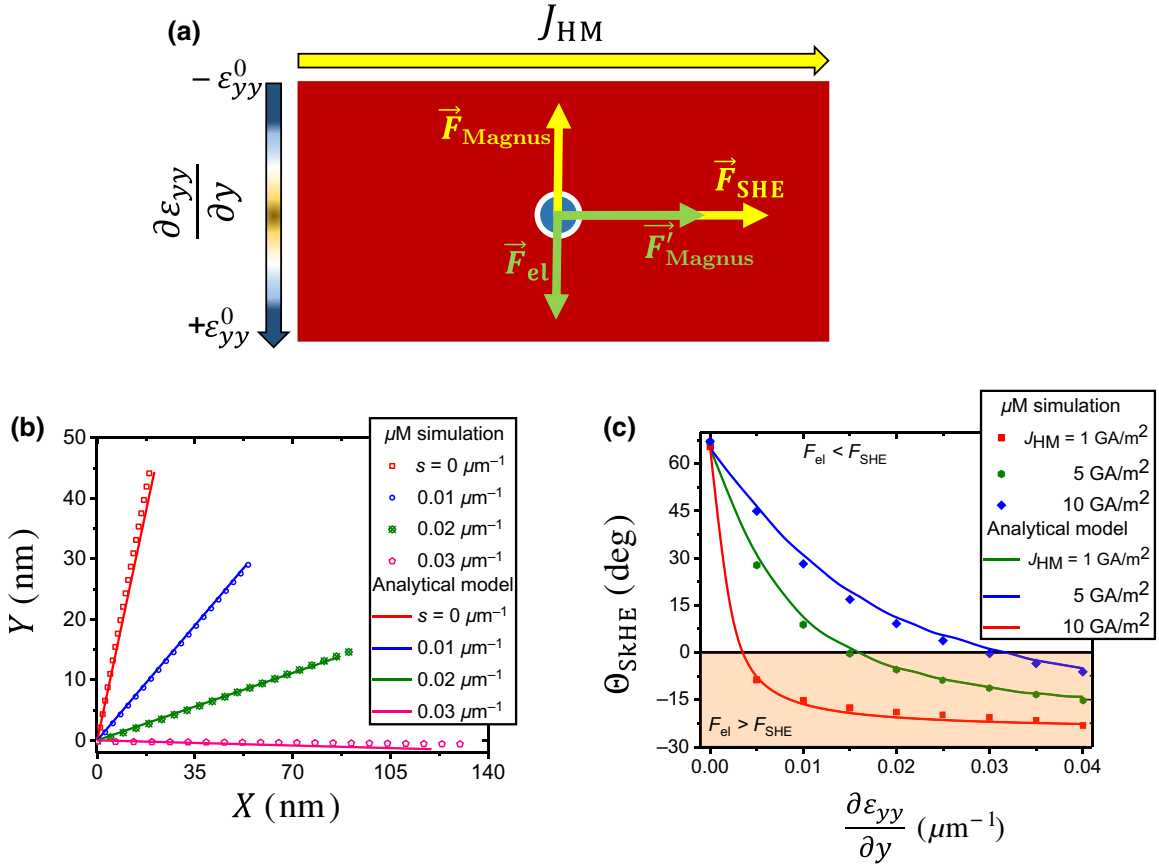

FIG. 3. (a) Schematic representation of the force contributions to skyrmion dynamics. (b) Skyrmion trajectories obtained from micromagnetic simulations (dots) and analytical calculations (lines) for a current density of $J_{HM} = 10$ GA/m^2 and different strain gradients. In the legend, "s" stands for "strain gradient" $s \equiv d\varepsilon_{yy}/dy$. (c) Evolution of the skyrmion Hall angle with strain gradient for different current-density values.

are also represented. Skyrmion dynamics in our system can be understood in terms of these four forces acting on it.

In addition to micromagnetic simulations, the well-known Thiele's model [34] can also give us useful information. In particular, analytical expressions for the forces involved can be derived. According to this model, under the action of $\vec{F}_{el}$ and $\vec{F}_{SHE}$, the skyrmion equation of motion is given by [34]

$$\vec{G} \times \vec{V} + \alpha \bar{\bar{D}} \vec{V} = \vec{F}_{SHE} + \vec{F}_{el}, \tag{2}$$

where $\vec{G} = -4\pi N_{sk}(\mu_0 M_s/\gamma_0) t_{FM} \vec{e}_z$ is the gyrovector, with $N_{sk} = -1$ as the skyrmion number; $\vec{V}$ is the skyrmion velocity; and

$$\bar{\bar{D}} = \begin{pmatrix} D_{xx} & D_{xy} \\ D_{yx} & D_{yy} \end{pmatrix}$$

is the dissipation tensor, with $D = D_{xx} = D_{yy} = -(\mu_0 \pi M_s/2\gamma_0) t_{FM}[\pi^2 - \mathrm{Ci}(2\pi) + \gamma_E + \log_{10}(2\pi)]$, and $D_{xy} = D_{yx} = 0$, with Ci and γ_E being the cosine integral function and Euler constant, respectively. The force due to the spin Hall effect is given by $\vec{F}_{SHE} = (\hbar \theta_{SH} J_{HM}/2|e|)\pi^2 \eta(\Delta/2)\vec{e}_x$, where θ_{SH} is the spin Hall angle, J_{HM} is the current density through the HM, $\Delta = 31$ nm is the skyrmion wall width, e is the electron charge, and η is a fitting parameter. On the other hand, the force due to the strain gradient is given by $\vec{F}_{el} = (3\pi\Delta^2 \lambda_s/8) t_{FM}(C_{11} + C_{12})(\partial \varepsilon_{yy}/\partial y)\vec{e}_y$ [13], where λ_s is the magnetostriction, $C_{11} = [Y(1-\upsilon)]/[(1+\upsilon)(1-2\upsilon)]$ and $C_{12} = \upsilon Y/[(1+\upsilon)/(1-2\upsilon)]$ are the elastic constants, and t_{FM} is the ferromagnetic layer thickness. All these terms are calculated using the zero-radius skyrmion ansatz described in Ref. [13].

From Eq. (2), the longitudinal and transversal components of the skyrmion velocity are given by

$$V_x = \frac{\alpha D F_{SHE} + G F_{el}}{\alpha^2 D^2 + G^2}, \tag{3}$$

$$V_y = \frac{-G F_{SHE} + \alpha D F_{el}}{\alpha^2 D^2 + G^2}, \tag{4}$$

so that the skyrmion Hall angle is given by

$$\theta_{SKHE} = \tan^{-1}\left(\frac{-G F_{SHE} + \alpha D F_{el}}{\alpha D F_{SHE} + G F_{el}}\right). \tag{5}$$

In Figs. 3(b) and 3(c), we show the predictions of the model (solid lines) together with the results of micromagnetic simulations (symbols). The same parameter values are used in both of them, with $\eta = 1.05$ as the only fitted parameter in Thiele's model. As can be observed, good quantitative agreement is found, which indicates that Thiele's model captures the most relevant features of skyrmion dynamics in our system. The discrepancies between the simulations and the model are mainly attributed to the fact that the skyrmion diameter depends on the strain [13,48] and, therefore, its diameter changes as it moves in the presence of a strain gradient, a feature not considered in Thiele's model.

Moreover, we can extract from the model the condition that needs to be satisfied for the skyrmion to move straight along the nanostrip without transversal deflection. By making either $V_y = 0$ in Eq. (4) or $\theta_{\mathrm{SKHE}} = 0$ in Eq. (5), we obtain

$$F_{\mathrm{el}} = \frac{G}{\alpha D} F_{\mathrm{SHE}}, \tag{6}$$

as the condition that guarantees the suppression of the skyrmion Hall effect. Using Eq. (6) and the expressions of F_{SHE} and F_{el} given above, we can obtain, for any given current density, J_{HM}, the value of the strain gradient, $\partial\varepsilon_{yy}/\partial y$ needed to cancel out the skyrmion Hall effect:

$$\frac{\partial \varepsilon_{yy}}{\partial y} = \frac{2\pi\ \eta\ G\ \hbar\ \theta_{\mathrm{SH}}}{3\alpha D|e|\Delta\ \lambda_s t_{\mathrm{FM}}(C_{11}+C_{12})} J_{\mathrm{HM}}. \tag{7}$$

Figure 4(a) shows the value of the strain gradient that cancels out the skyrmion Hall effect for different values of the applied current density, as obtained from micromagnetic simulations (green symbols) and from Eq. (7) (red line). Again, excellent agreement is found between them. The discrepancies are even smaller than those in Figs. 3(b) and 3(c) because now the skyrmion moves horizontally, which is perpendicular to the strain gradient, and, therefore, its diameter does not change during motion [13,48].

On the other hand, in Fig. 4(b), we plot the skyrmion speed as a function of the current density obtained from micromagnetic simulations both without a strain gradient (green symbols) and with the strain gradient that cancels out the skyrmion Hall effect (red symbols). The corresponding values obtained from Thiele's model are also shown with solid lines (orange and blue, respectively). As can be observed, a linear increase in the longitudinal velocity (V_x) is obtained in both cases, but the speed values are remarkably higher when the strain gradient is included. This can be understood by considering that $\vec{F}'_{\mathrm{Magnus}}$, the Magnus force associated with $\vec{F}_{\mathrm{el}}$, points along the positive x axis [see Fig. 3(a) and Eq. (3)] and, as a result, it adds up to $\vec{F}_{\mathrm{SHE}}$, increasing the total force and pushing

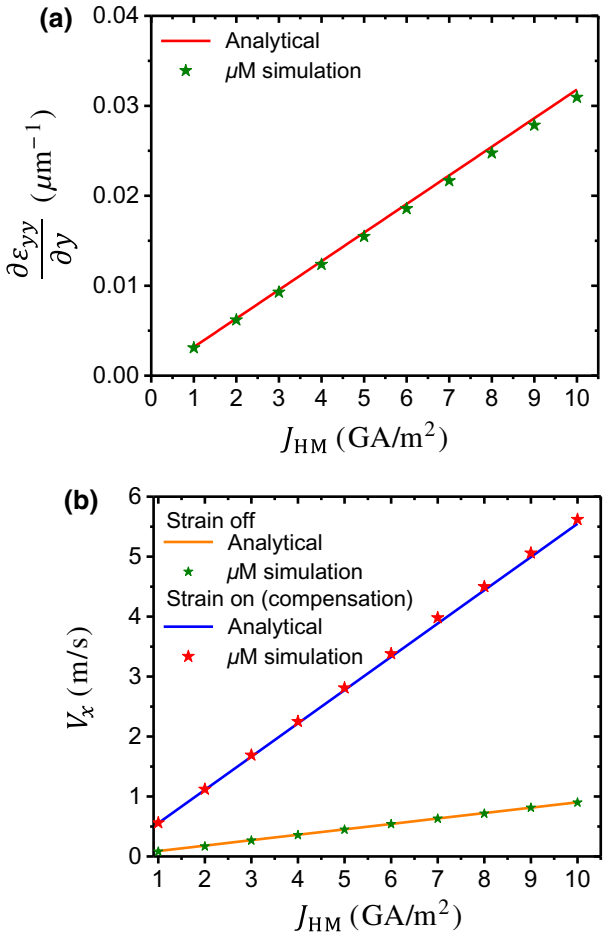

FIG. 4. (a) Strain-gradient slope required to compensate for the skyrmion Hall angle for each current-density, J_{HM}, value. (b) Skyrmion speed versus applied current in the absence of strain and in the presence of a strain compensating for the skyrmion Hall angle.

the skyrmion along the nanostrip. Therefore, by choosing an appropriate value of the strain gradient, which depends linearly on the applied voltage, it is possible not only to suppress the skyrmion Hall effect but also to increase its velocity significantly.

Up to now, we have shown that our scheme for tuning the skyrmion Hall angle works for idealized samples, but it remains to be seen if it would also work in real samples, where intrinsic pinning due to structural disorder is known to play an important role in skyrmion dynamics [49]. With that goal in mind, we carry out simulations with the same geometry and material parameter values described before but now including disorder [50]. Disorder is modeled via a Voronoi tessellation of the film in polygonal regions of average diameter, $d = 5$ nm, where both the anisotropy constant and easy-axis orientation are different for each grain, following a Gaussian distribution around their nominal values, $K_u = 0.8$ MJ/m^3 and $\vec{u}_k = \{0, 0, 1\}$, with standard deviation $\sigma = 2\%$ [51]. The

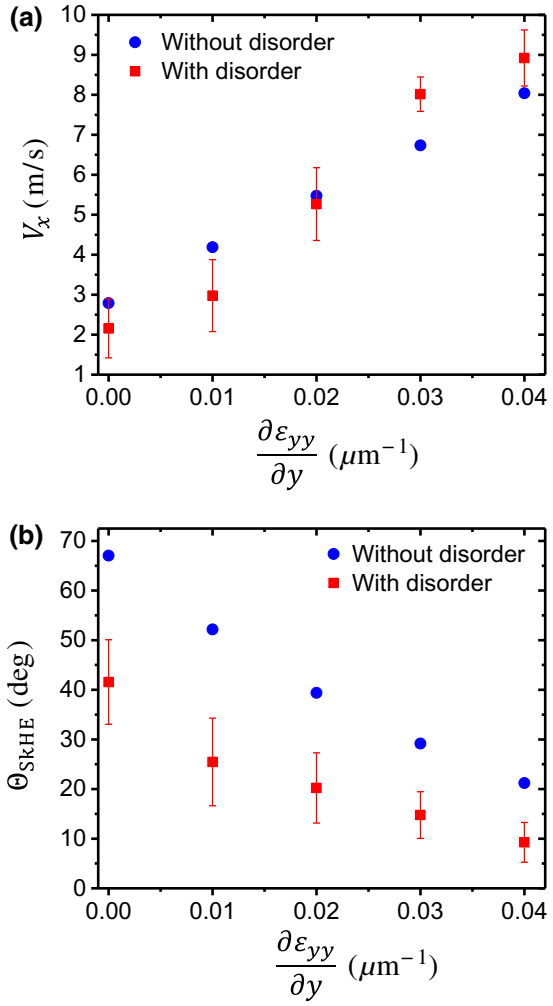

FIG. 5. (a) Skyrmion speed versus strain gradient for a disordered FM film (red dots) and for an ideal FM film (blue dots). (b) Skyrmion Hall angle evolution versus strain gradient for a disordered FM film (red dotes) and for an ideal FM film (blue dots). Graphs show a comparison between disordered and ideal films in the presence of a current density of $J_{HM} = 30$ GA/m^2.

results are shown in Fig. 5 together with those carried out in the absence of disorder for an applied current density of $J_{HM} = 30$ GA/m^2. This value is well above the range investigated in Fig. 3 because we are mainly interested in the flow regime [49,52].

Both the skyrmion speed [Fig. 5(a)] and skyrmion Hall angle [Fig. 5(b)] as a function of the strain gradient are plotted. In the simulations with disorder (red squares), the results are obtained by averaging over 10 realizations, each one with a different grain distribution. As can be observed in Fig. 5(a), the increase in the skyrmion speed with the strain gradient remains in the presence of disorder. On the other hand, disorder leads to a reduction in the skyrmion Hall angle [Fig. 5(b)] [52–55], but also a monotonous decrease with the strain gradient is obtained, as it is the case without disorder. Animations of skyrmion motion in the presence of disorder are presented in the Supplemental Material [56].

Although the results shown in the manuscript are obtained without considering thermal fluctuations in the simulations, some trials are made at a finite temperature, and the results do not show a significant effect on the skyrmion Hall angle for the current-density range considered. In a recent publication [57], it was shown that the skyrmion Hall angle was not significantly affected by temperature, unless a high-flow regime was reached, where some distortion on the skyrmion structure took place. A previous computational study [58] showed that the effect of temperature on the skyrmion Hall angle was most pronounced at small driving forces where thermally induced depinning occurred, whereas in the flow regime it slightly increased with temperature.

As pointed out before, in narrow nanostrips, the edges exert a repulsive force on the skyrmions that affect their dynamics. In particular, this force increases as the skyrmion deviates from the center ($y = 0$) and, at some point, it compensates for the Magnus force due to the current, and the skyrmion ends up in a horizontal trajectory at a given distance, y_{term}, from the nanostrip central axis. However, for current densities above a certain critical value, J_c, the edge repulsion is not strong enough to compensate for the Magnus force and the skyrmion is annihilated at the edge. This critical value, which depends on the nanowire's width, limits the current range of device operability. In this last part of the manuscript, we explore how our approach can be used to increase this critical current. To do that, we simulate a nanostrip of dimensions $1024 \times 128 \times 1$ nm^3, which is narrower but with the same material parameter values as that of the one considered before [Fig. 1(a)]. Thiele's model is also used by including an additional force in Eq. (2) that considers repulsion from the edges, $\vec{F}_{rep}$. Following previous works [59], it is modeled as $\vec{F}_{rep} = k\, Y(t)\, \vec{e}_y$, where $k = 3.6\ 10^{-5}$ N/m is an elastic constant estimated from micromagnetic simulations and $Y(t)$ is the skyrmion's transversal position. The dynamic equation, Eq. (2), with the new term $\vec{F}_{rep}$ can be solved analytically, yielding

$$X(t) = \frac{F_{SHE}}{\alpha D} t + \frac{G^2 F_{SHE} + G\alpha D F_{el}}{\alpha^2 D^2 k}[1 - e^{-(t/\tau)}], \quad (8)$$

$$Y(t) = \frac{G F_{SHE} - \alpha D F_{el}}{\alpha D k}[1 - e^{-(t/\tau)}], \quad (9)$$

where $\tau = (G^2 + \alpha^2 D^2)/\alpha D k$ is the characteristic time for the skyrmion response to the edge force.

In Fig. 6, we show the skyrmion trajectory for a time window of 25 ns and different values of the applied current density without strain gradient [Fig. 6(a)] and for a strain gradient of $\partial \varepsilon_{yy}/\partial y = 0.08\ \mu$m^{-1} [Fig. 6(b)]. The trajectories obtained from both micromagnetic simulations and Thiele's model are shown. As can be observed

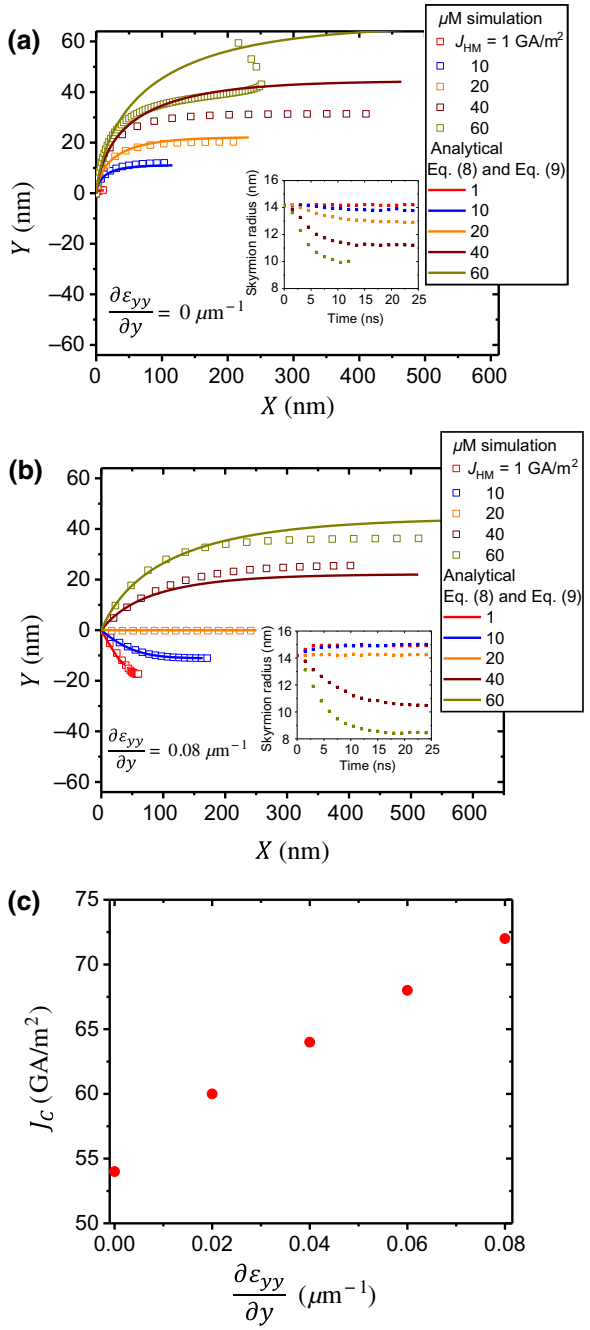

FIG. 6. Skyrmion trajectory for different applied current densities (a) without and (b) in the presence of a strain gradient. Both the results of micromagnetic simulations (symbols) and Thiele's model (lines) are shown. Time evolution of the skyrmion radius is shown in the insets. (c) Threshold current for skyrmion annihilation as a function of the strain gradient.

in Fig. 6(a), the terminal vertical displacement of the skyrmion increases with the current density and, for the largest one, $J_{\mathrm{HM}} = 60$ GA/m^2, the skyrmion is annihilated when it hits the boundary [$Y = w_{\mathrm{FM}}/2 = 64$ nm]. This terminal displacement is significantly reduced when the strain gradient is applied [Fig. 6(b)], up to the point that, for the smallest current-density values, it is negative. This makes it possible for a current of $J_{\mathrm{HM}} = 60$ GA/m^2 and higher to be injected without the skyrmion being annihilated. Micromagnetic simulation and Thiele's model predict very similar behavior. The discrepancies between them are mainly attributed to the fact that the skyrmion's radius changes as it moves vertically, as shown in the insets of Figs. 6(a) and 6(b), and to the fact that repulsion from the edges is not accurately described with an elastic force when the skyrmion is close to the edge [60]. In Fig. 6(c), we show the maximum current, J_c, that can be injected without the skyrmion being annihilated at the edge of the nanostrip for different values of $\partial \varepsilon_{yy}/\partial y$. As can be observed, J_c increases with the strain gradient, which proves that our approach can be used to inject higher currents in the nanostrip, with the consequent increase in speed and operating range of the devices.

III. CONCLUSIONS

We show a route to control the skyrmion trajectory and cancel out the skyrmion Hall effect via an electric field in hybrid piezoelectric-magnetic multilayers. We investigate the electromechanical response of the device when a voltage is applied between two lateral electrodes, finding a transversal strain gradient in the central part of the ferromagnetic layer, the amplitude of which is linear with the applied voltage and with the inverse of the distance between the electrodes. Micromagnetic simulations show that such a strain gradient leads to a transverse force on the skyrmion that can have a sizable effect on its trajectory when driven by a current. In particular, the skyrmion Hall effect can be cancelled out for any given current density if a proper voltage is applied. Moreover, the strain gradient contributes to increasing the longitudinal velocity and, in narrow nanostrips, it allows for an increase of the maximum current density that can be injected before the skyrmion is annihilated at the nanostrip edge. Our approach works under realistic conditions, in particular, in the presence of structural disorder in the ferromagnet. From a broader perspective, we believe that the applicability of our approach goes beyond the possibility of cancelling out the skyrmion Hall angle, but it provides additional degrees of freedom to control skyrmion motion, which could have a strong impact on the design of skyrmion-based memories and logic and neuromorphic computing devices.

ACKNOWLEDGMENTS

We gratefully acknowledge financial support from the European Union H2020 Program (MSCA MagnEFi ITN Grant No. 860060), from the Ministerio de Education y Ciencia (Project No. MAT2017-87072-C4-1-P), from the Ministerio de Ciencia e Innovacion (Project No. PID2020-117024GB-C41), and from the Consejeria de Educación

of Castilla y León (Projects No. SA114P20 and No. SA299P18). We thank Liza Herrera-Diez and Guillaume Agnus for fruitful discussions about the experimental realization of our device.

[1] S. Mühlbauer, B. Binz, F. Jonietz, C. Pfleiderer, A. Rosch, A. Neubauer, R. Georgii, and P. Böni, Skyrmion lattice in a chiral magnet, Science **323**, 915 (2009).

[2] Maverick Chauwin, Xuan Hu, Felipe Garcia-Sanchez, Neilesh Betrabet, Alexandru Paler, Christoforos Moutafis, and Joseph S. Friedman, Skyrmion Logic System for Large-Scale Reversible Computation, Phys. Rev. Appl. **12**, 064053 (2019).

[3] Zhizhong Zhang, Yuanzhi Zhu, Yue Zhang, Kun Zhang, Jiang Nan, Zhenyi Zheng, Youguang Zhang, and Weisheng Zhao, Skyrmion-based ultra-low power electric-field-controlled reconfigurable (SUPER) logic gate, IEEE Trans. Electron Devices **40**, 1984 (2019).

[4] Shijiang Luo, Min Song, Xin Li, Yue Zhang, Jeongmin Hong, Xiaofei Yang, Xuecheng Zou, Nuo Xu, and Long You, Reconfigurable skyrmion logic gates, Nano Lett. **18**, 1180 (2018).

[5] Mouad Fattouhi, Kai Yu Mak, Yan Zhou, Xichao Zhang, Xiaoxi Liu, and Mohamed El Hafidi, Logic Gates Based on Synthetic Antiferromagnetic Bilayer Skyrmions, Phys. Rev. Appl. **16**, 014040 (2021).

[6] X. Chen, H. Zhang, E. Deng, M. Yang, N. Lei, Y. Zhang, W. Kang, and W. Zhao, Sky-RAM: Skyrmionic random access memory, IEEE Electron Device Lett. **40**, 722 (2019).

[7] R. Tomasello, E. Martinez, R. Zivieri, L. Torres, M. Carpentieri, and G. Finocchio, A strategy for the design of skyrmion racetrack memories, Sci. Rep. **4**, 6784 (2014).

[8] Kyung Mee Song, Jae-Seung Jeong, Biao Pan, Xichao Zhang, Jing Xia, Sunkyung Cha, Tae-Eon Park, Kwangsu Kim, Simone Finizio, Jörg Raabe, Joonyeon Chang, Yan Zhou, Weisheng Zhao, Wang Kang, Hyunsu Ju, and Seonghoon Woo, Skyrmion-based artificial synapses for neuromorphic computing, Nat. Electron **3**, 148 (2020).

[9] Diana Prychynenko, Matthias Sitte, Kai Litzius, Benjamin Krüger, George Bourianoff, Mathias Kläui, Jairo Sinova, and Karin Everschor-Sitte, Magnetic Skyrmion as a Nonlinear Resistive Element: A Potential Building Block for Reservoir Computing, Phys. Rev. Appl. **9**, 014034 (2018).

[10] G. Finocchio, M. Ricci, R. Tomasello, A. Giordano, M. Lanuzza, V. Puliafito, P. Burrascano, B. Azzerboni, and M. Carpentieri, Skyrmion based microwave detectors and harvesting, Appl. Phys. Lett. **107**, 262401 (2015).

[11] Albert Fert, Vincent Cros, and João Sampaio, Skyrmions on the track, Nat. Nano **8**, 152 (2013).

[12] R. Tomasello, S. Komineas, G. Siracusano, M. Carpentieri, and G. Finocchio, Chiral skyrmions in an anisotropy gradient, Phys. Rev. B **98**, 024421 (2018).

[13] R. Yanes, F. Garcia-Sanchez, R. F. Luis, E. Martinez, V. Raposo, L. Torres, and L. Lopez-Diaz, Skyrmion motion induced by voltage-controlled in-plane strain gradients, Appl. Phys. Lett. **115**, 132401 (2019).

[14] Rabindra Nepala, Utkan Güngördü, and Alexey A. Kovalev, Magnetic skyrmion bubble motion driven by surface acoustic waves, Appl. Phys. Lett. **112**, 112404 (2018).

[15] J. J. Liang, J. H. Yu, J. Chen, M. H. Qin, M. Zeng, X. B. Lu, X. S. Gao, and J.-M. Liu, Magnetic field gradient driven dynamics of isolated skyrmions and antiskyrmions in frustrated magnets, New J. Phys. **20**, 053037 (2018).

[16] Sai Li, Jing Xia, Xichao Zhang, Motohiko Ezawa, Wang Kang, Xiaoxi Liu, Yan Zhou, and Weisheng Zhao, Dynamics of a magnetic skyrmionium driven by spin waves, Appl. Phys. Lett. **112**, 142404 (2018).

[17] Lingyao Kong and Jiadong Zang, Dynamics of an Insulating Skyrmion Under a Temperature Gradient, Phys. Rev. Lett. **111**, 067203 (2013).

[18] K. Litzius, I. Lemesh, B. Krüger, P. Bassirian, L. Caretta, K. Richter, F. Büttner, K. Sato, O. A. Tretiakov, J. Förster, R. M. Reeve, M. Weigand, I. Bykova, H. Stoll, G. Schütz, G. S. D. Beach, and M. Kläui, Skyrmion Hall effect revealed by direct time-resolved X-ray microscopy, Nat. Phys. **13**, 170 (2017).

[19] Wanjun Jiang, Xichao Zhang, Guoqiang Yu, Wei Zhang, Xiao Wang, M. Benjamin Jungfleisch, John E. Pearson, Xuemei Cheng, Olle Heinonen, Kang L. Wang, Yan Zhou, Axel Hoffmann, and Suzanne G. E. te Velthuis, Direct observation of the skyrmion Hall effect, Nat. Phys. **13**, 162 (2017).

[20] Börge Göbel and Ingrid Mertig, Skyrmion ratchet propagation: Utilizing the skyrmion Hall effect in AC racetrack storage devices, Sci. Rep. **11**, 3020 (2021).

[21] C. Reichhardt and C. J. O. Reichhardt, Plastic flow and the skyrmion Hall effect, Nat. Commun. **11**, 738 (2020).

[22] Anthony K. C. Tan, Pin Ho, James Lourembam, Lisen Huang, Hang Khume Tan, Cynthia J. O. Reichhardt, Charles Reichhardt, and Anjan Soumyanarayanan, Visualizing the strongly reshaped skyrmion Hall effect in multilayer wire devices, Nat. Commun. **12**, 4252 (2020).

[23] Barton L. Brown, Uwe C. Täuber, and Michel Pleimling, Effect of the Magnus force on skyrmion relaxation dynamics, Phys. Rev. B **97**, 020405(R) (2018).

[24] H. Velkov, O. Gomonay, M. Beens, G. Schwiete, A. Brataas, J. Sinova, and R. A. Duine, Phenomenology of current-induced skyrmion motion in antiferromagnets, New J. Phys. **18**, 075016 (2016).

[25] Joseph Barker and Oleg A. Tretiakov, Static and dynamical properties of antiferromagnetic skyrmions in the presence of applied current and temperature, Phys Rev Let **116**, 147203 (2016).

[26] Xichao Zhang, Yan Zhou, and Motohiko Ezawa, Magnetic bilayer-skyrmions without skyrmion Hall effect, Nat. Comm. **7**, 10293 (2016).

[27] William Legrand, Davide Maccariello, Fernando Ajejas, Sophie Collin, Aymeric Vecchiola, Karim Bouzehouane, Nicolas Reyren, Vincent Cros, and Albert Fert, Room-temperature stabilization of antiferromagnetic skyrmions in synthetic antiferromagnets, Nat. Mater. **19**, 34 (2020).

[28] Takaaki Dohi, Samik Dutta-Gupta, Shunsuke Fukami, and Hideo Ohno, Formation and current-induced motion of synthetic antiferromagnetic skyrmion bubbles, Nat. Commun. **10**, 5153 (2019).

[29] Laichuan Shen, Xiaoguang Li, Yuelei Zhao, Jing Xia, Guoping Zhao, and Yan Zhou, Current-Induced Dynamics of the Antiferromagnetic Skyrmion and Skyrmionium, Phys. Rev. Appl. **12**, 064033 (2019).

[30] Xichao Zhang, Jing Xia, Yan Zhou, Daowei Wang, Xiaoxi Liu, Weisheng Zhao, and Motohiko Ezawa, Control and

manipulation of a magnetic skyrmionium in nanostructures, Phys. Rev. B **94**, 094420 (2016).

[31] Yue Zhang, Shijiang Luo, Baiqian Yan, Jun Ou-Yang, Xiaofei Yang, Shi Chen, Benpeng Zhu, and Long You, Magnetic skyrmions without the skyrmion Hall effect in a magnetic nanotrack with perpendicular anisotropy, Nanoscale **9**, 10212 (2017).

[32] Collins Ashu Akosa, Hang Li, Gen Tatara, and Oleg A. Tretiakov, Tuning the Skyrmion Hall Effect via Engineering of Spin-Orbit Interaction, Phys. Rev. Appl. **12**, 054032 (2019).

[33] Börge Göbel, Alexander Mook, Jürgen Henk, and Ingrid Mertig, Overcoming the speed limit in skyrmion racetrack devices by suppressing the skyrmion Hall effect, Phys. Rev. B **99**, 020405(R) (2019).

[34] A. A. Thiele, Steady-State Motion of Magnetic Domains, Phys. Rev. Lett. **30**, 230 (1973).

[35] COMSOL MULTIPHYSICS user's guide (4.3 ed), COMSOL Multiphysics AB. (www.comsol.com).

[36] S. J. A. Koh, H. P. Lee, C. Lu, and Q. H. Cheng, Molecular dynamics simulation of a solid platinum nanowire under uniaxial tensile strain: Temperature and strain-rate effects, Phys. Rev. B **72**, 085414 (2005).

[37] A. T. Hindmarch, A. W. Rushforth, R. P. Campion, C. H. Marrows, and B. L. Gallagher, Origin of in-plane uniaxial magnetic anisotropy in CoFeB amorphous ferromagnetic thin films, Phys. Rev. B **83**, 212404 (2011).

[38] Chang-Sheng Zha, Ho-kwang Mao, and Russell J. Hemley, Elasticity of MgO and a primary pressure scale to 55 GPa, PNAS **97**, 1349 (2000).

[39] M. Azize and T. Palacios, Effect of substrate-induced strain in the transport properties of AlGaN/GaN heterostructures, J. Appl. Phys. **108**, 023707 (2010).

[40] Arne Vansteenkiste, Jonathan Leliaert, Mykola Dvornik, Mathias Helsen, Felipe Garcia-Sanchez, and Bartel Van Waeyenberge, The design and verification of MuMax^3, AIP Adv. **4**, 107133 (2014).

[41] J. C. Slonczewski, Current-driven excitation of magnetic multilayers, J. Magn. Magn. Mater. **159**, L1 (1996).

[42] Stanisław Łazarski, Witold Skowroński, Krzysztof Grochot, Wiesław Powroźnik, Jarosław Kanak, Marek Schmidt, and Tomasz Stobiecki, Spin-orbit torque induced magnetization dynamics and switching in a CoFeB/Ta/CoFeB system with mixed magnetic anisotropy, Phys. Rev. B **103**, 134421 (2021).

[43] I. Benguettat-El Mokhtari, D. Ourdani, Y. Roussigne, R. B. Mos, M. Nasui, S. M. Cherif, A. Stachkevich, M. S. Gabor, and M. Belmeguenai, Investigation of the correlation between perpendicular magnetic anisotropy, spin mixing conductance and interfacial Dzyaloshinskii–Moriya interaction in CoFeB-based systems, J. Phys. D: Appl. Phys. **53**, 505003 (2020).

[44] L. Herrera Diez, F. García-Sánchez, J.-P. Adam, T. Devolder, S. Eimer, M. S. El Hadri, A. Lamperti, R. Mantovan, B. Ocker, and D. Ravelosona, Controlling magnetic domain wall motion in the creep regime in He^+-irradiated CoFeB/MgO films with perpendicular anisotropy, Appl. Phys. Lett. **107**, 032401 (2015).

[45] Jia-Mian Hu, Tiannan Yang, and Long-Qing Chen, Strain-mediated voltage-controlled switching of magnetic skyrmions in nanostructures, npj Comput. Mater. **4**, 62 (2018).

[46] M. Gueye, F. Zighem, M. Belmeguenai, M. S. Gabor, C. Tiusan, and D. Faurie, Spectroscopic investigation of elastic and magnetoelastic properties of CoFeB thin films, J. Phys. D: Appl. Phys. **49**, 145003 (2016).

[47] L. Herrera Diez, M. Voto, A. Casiraghi, M. Belmeguenai, Y. Roussigné, G. Durin, A. Lamperti, R. Mantovan, V. Sluka, V. Jeudy, Y. T. Liu, A. Stashkevich, S. M. Chérif, J. Langer, B. Ocker, L. Lopez-Diaz, and D. Ravelosona, Enhancement of the dzyaloshinskii-moriya interaction and domain wall velocity through interface intermixing in Ta/CoFeB/MgO, Phys. Rev. B **99**, 054431 (2019).

[48] Philippa M Shepley, Gavin burnell and Tom. A moore, domain wall energy and strain in Pt/Co/Ir thin films on piezoelectric transducers, J. Phys: Condens. Matter **30**, 344002 (2018).

[49] Joo-Von Kim and Myoung-Woo Yoo, Current-driven skyrmion dynamics in disordered films, Appl. Phys. Lett. **110**, 132404 (2017).

[50] J. Leliaert, B. Van de Wiele, A. Vansteenkiste, L. Laurson, G. Durin, L. Dupré, and B. Van Waeyenberge, Current-driven domain wall mobility in polycrystalline permalloy nanowires: A numerical study, J. Appl. Phys. **115**, 233903 (2014).

[51] Oscar Alejos, Victor Raposo, Luis Sanchez-Tejerina, Riccardo Tomasello, Giovanni Finocchio, and Eduardo Martinez, Current-driven domain wall dynamics in ferromagnetic layers synthetically exchange-coupled by a spacer: A micromagnetic study, J. Appl. Phys. **123**, 013901 (2018).

[52] Roméo Juge, *et al.*, Current-Driven Skyrmion Dynamics and Drive-Dependent Skyrmion Hall Effect in an Ultrathin Film, Phys. Rev. Appl. **12**, 044007 (2019).

[53] C. Reichhardt, D. Ray, and C. J. Olson Reichhardt, Collective Transport Properties of Driven Skyrmions with Random Disorder, Phys. Rev. Lett. **114**, 217202 (2015).

[54] C. Reichhardt and C. J. Olson Reichhardt, Noise fluctuations and drive dependence of the skyrmion Hall effect in disordered systems, New J. Phys. **18**, 095005 (2016).

[55] C. Reichhardt, C. J. O. Reichhardt, and M. V. Milosevic, *Statics and Dynamics of Skyrmions Interacting with Pinning: A Review*, arXiv:2102.10464 [cond-mat.mes-hall].

[56] See the Supplemental Material at http://link.aps.org/supplemental/10.1103/PhysRevApplied.16.044035 for further information regarding skyrmion motion in disorder.

[57] Kai Litzius, Jonathan Leliaert, Pedram Bassirian, Davi Rodrigues, Sascha Kromin, Ivan Lemesh, Jakub Zazvorka, Kyu-Joon Lee, Jeroen Mulkers, Nico Kerber, Daniel Heinze, Niklas Keil, Robert M. Reeve, Markus Weigand, Bartel Van Waeyenberge, Gisela Schütz, Karin Everschor-Sitte, Geoffrey S. D. Beach, and Mathias Kläui, The role of temperature and drive current in skyrmion dynamics, Nat Electron **3**, 30 (2020).

[58] C. Reichhardt and C. J. Olson Reichhardt, Thermal creep and the skyrmion Hall angle in driven skyrmion crystals, J. Phys: Condens. Matter **31**, 07LT01 (2019).

[59] Victor Raposo, Ricardo francisco luis martinez, and eduardo martinez, current-driven skyrmion motion along disordered magnetic tracks, AIP Adv. **7**, 056017 (2017).

[60] J. C. Martinez, W. S. Lew, W. L. Gan, and M. B. A. Jalil, Theory of current-induced skyrmion dynamics close to a boundary, J. Magn. Magn. Mater. **465**, 685 (2018).